Evolution and performances of Ni single atoms trapped by mesoporous ceria in Dry Reforming of Methane

Jiwei Li [a], Congcong Du [a,b], Qingyue Feng [a], Yiran Zhao [a,b], Sixu Liu [b], Junli Xu [b], Min Hu [e], Zizhen Zeng [a], Zhun Zhang [a,b], Hongxia Shen [d], Yuxuan Zhang [f], Jianqiu Zhu [f], Linjuan Zhang [f], Wei Zhao [e,*], Jianyu Huang [c,*], Haifeng Xiong [a,b,**]

[a] State Key Laboratory of Physical Chemistry of Solid Surfaces, College of Chemistry and Chemical Engineering, Xiamen University, 422 Siming South Road, Xiamen 361005, China
[b] Innovation Laboratory for Sciences and Technologies of Energy Materials of Fujian Province, Xiamen 361102, China
[c] Clean Nano Energy Center, State Key Laboratory of Metastable Materials Science and Technology, Yanshan University, Qinhuangdao 066004, China
[d] College of Biological, Chemical Sciences and Engineering, Jiaxing University, Jiaxing, Zhejiang 314001, China
[e] Institute for Advanced Study, Shenzhen University, Shenzhen 518060, China
[f] Key Laboratory of Interfacial Physics and Technology, Shanghai Institute of Applied Physics, Chinese Academy of Sciences, Shanghai 201008, China

ARTICLE INFO

ABSTRACT

Bulk ceria can stabilize metal single atoms in oxidizing conditions. However, the obtained catalysts undergo sintering at high temperatures, due to the poor stability of the support. In this work, we prepared ordered mesoporous ceria (mp-CeO_2) to trap Ni single atoms in dry reforming of CH_4 (DRM). We found that the Ni_1@mp-CeO_2 catalyst presented many oxygen vacancies (O_V) and basic sites, helping to activate CO_2 and generate reactive oxygen to remove carbon deposits, as compared to a Ni_1/CeO_2 sample prepared by impregnation. Moreover, the confinement of mesoporous CeO_2 prevents the sintering of Ni clusters derived from Ni single atoms and enhances the stability of the catalyst. The Ni_1@mp-CeO_2 catalyst has a higher CH_4 conversion, and less deactivation rate, as compared to the Ni_1/CeO_2. This work demonstrates Ni single atoms undergo growth to nanoclusters in DRM and the use of Ni single atoms as catalyst precursor can suppress the carbon deposition.

1. Introduction

Metal single-atom catalysts (SACs) have attracted extensive attentions due to the maximum metal atom utilization and unique catalytic reactivity in heterogeneous catalysis [1–4]. SACs can be achieved by constructing strong metal-support interaction or increasing the support defects, which were used to confine or anchor metal atoms [5–8]. Currently, SACs have been successfully synthesized on various supports via different methods, including wet chemistry, atom trapping, atomic layer deposition, vapor-phase self-assembly and others [9–13]. Most of these as-synthesized SACs are stable at temperatures of < 200 °C due to the formation of metal-support bond and some metal SACs can even withstand the temperatures up to 800 °C in oxidizing conditions [14, 15]. However, the stability of the metal SACs in reducing conditions has been barely studied because the ionic metal can be reduced,

subsequently leading to the agglomeration of single atoms [16–19]. Therefore, novel approaches need be developed to improve the stability and catalytic performances of metal SACs at elevated temperatures in a reducing environment, e.g., for the important reaction dry reforming of methane (DRM).

Dry reforming of methane can convert two greenhouse gas molecules, CH_4 and CO_2, into syngas (CO and H_2), which can be used to produce value-added liquid fuels and chemicals via the mature syngas chemistry [20–22]. In this process, catalyst sintering and carbon deposition are the two main reasons for the catalyst deactivation at high temperatures. Previous studies have demonstrated an intimate correlation between carbon deposition and nickel particle size, showing that the small Ni particle can weaken the driving force of carbon diffusion and thereby remarkably suppress the carbon deposition [23]. It is therefore reasonable to assume that Ni single-atom catalyst would

---

* Corresponding author.
** Corresponding author at: State Key Laboratory of Physical Chemistry of Solid Surfaces, College of Chemistry and Chemical Engineering, Xiamen University, 422 Siming South Road, Xiamen 361005, China.
E-mail addresses: weizhao@szu.edu.cn (W. Zhao), jhuang@ysu.edu.cn (J. Huang), haifengxiong@xmu.edu.cn (H. Xiong).

generate negligible amount of carbon deposits [17,24]

CeO$_2$ supports are unique supports for catalysis due to abundant oxygen vacancies and the excellent redox properties [25]. On the other hand, CeO$_2$ can be used as support to trap metal single atoms to form the atomically dispersed catalysts (M$_1$/CeO$_2$) because of the strong metal-support interaction [26,27]. For example, Pt$_1$/CeO$_2$ SAC can be obtained by directly dispersing Pt salt precursors onto the ceria, followed by annealing the material at elevated temperatures in air [10,28]. However, bulk CeO$_2$ powder has poor thermal stability, and the structure is prone to collapse at elevated temperatures, leading to the dramatical decrease in surface area and poor activity [16]. Compared with bulk CeO$_2$, highly ordered mesoporous CeO$_2$ has large surface area, interconnected channels and ordered mesoporous structures, showing the improved stability at high temperatures. Mesoporous CeO$_2$ (mp-CeO$_2$) nanomaterials can be obtained via hydrothermal method, microwave method, hard template method (KIT-6 and SBA-15) and others [29–32]. These ordered mesoporous mp-CeO$_2$ have the uniform size pores used to confine single atoms and therefore has the potent to further stabilize metal single atoms.

In this work, we employed mesoporous CeO$_2$ to trap Ni single atoms (Ni$_1$@mp-CeO$_2$) and investigated the stability, evolution and the catalytic performances of the trapped single atom catalyst during DRM (CH$_4$ and CO$_2$) at elevated temperatures. In addition, the Ni$_1$@mp-CeO$_2$ catalyst was compared with an impregnated Ni$_1$/CeO$_2$ catalyst supported on bulk CeO$_2$ powder obtained by calcining cerium nitrate. The stability, evolution and carbon deposits of the single-atom catalyst were discussed in DRM.

2. Experimental section

2.1. Chemicals and materials

Cerium (III) nitrate hexahydrate (Ce(NO$_3$)$_3$·6 H$_2$O, AR), Pluronic P123 triblock copolymer (EO$_{20}$PO$_{70}$EO$_{20}$), were purchased from Sigma-Aldrich Chemical Reagent Co., Ltd. Tetraethyl orthosilicate (TEOS, 99%), Hydrochloric acid (HCl, $\geq$ 36.5%, AR), Ethanol (C$_2$H$_5$OH, AR), Sodium hydroxide (NaOH, AR), Nickel nitrate hexahydrate (Ni (NO$_3$)$_2$·6 H$_2$O, AR), were obtained from Sinopharm Chemical Reagent Co., Ltd.

2.2. Catalyst preparation

The ordered mesoporous CeO$_2$ was synthesized using SBA-15 silica as hard template, following similar methods to those in previous studies [32,33]. First, SBA-15 silica was prepared by dissolving Pluronic P123 triblock copolymer in an HCl aqueous solution (1.6 M) and subsequently adding tetraethyl orthosilicate (TEOS) at 40 ℃. After 24 h of stirring, the mixed solution was hydrothermally treated in a Teflon-lined stainless steel autoclave at 100 ℃ for 48 h, followed by filtration, washing, drying at 80 ℃, and calcination at 550 ℃ for 6 h to obtain SBA-15. Next, 1 g of SBA-15 was added into 10 mL ethanol solution in which contained 10.8 mmol of Ce(NO$_3$)$_3$·6 H$_2$O, and then stirred at 35 ℃ until the complete evaporation of ethanol before calcination at 350 ℃ for 3 h. The sample was then repeatedly impregnated with 3.8 mmol of Ce (NO$_3$)$_3$·6 H$_2$O in 10 mL ethanol solution. After ethanol evaporation, the obtained powder was calcined at 750 ℃ for 3 h. Finally, SBA-15 hard template was removed by NaOH solution (2 M) for three times and washed by deionized water. The final product was dried at 80 ℃ to obtain mesoporous CeO$_2$ (mp-CeO$_2$). For comparison, a powder CeO$_2$ support (denoted as CeO$_2$) was obtained by calcining Ce(NO$_3$)$_3$·6 H$_2$O at 350 ℃ for 6 h. The mesoporous CeO$_2$ supported Ni catalyst was prepared by impregnation and for the purpose of comparison, a reference Ni$_1$/CeO$_2$ catalyst was prepared by impregnating nickel nitrate onto the CeO$_2$, followed by drying and calcining. After impregnating nickel nitrate solution onto the supports of CeO$_2$ or mp-CeO$_2$, the mixture was dried at 60 ℃ for 12 h. Finally, the catalyst was calcined at 450 ℃ for 3 h in static air atmosphere in a muffle.

2.3. Catalyst characterization

Powder X-ray diffraction (XRD) patterns were recorded using a PANalytical X'pert PRO diffractometer with a Cu Kα radiation. N$_2$ physical adsorption and desorption experiments of these catalysts, after degassed for 4 h at 150 ℃, were tested using the Micromeritics Tri-Star II 3020. Scanning electron microscopy (SEM) images and transmission electron microscopy (TEM) images were obtained from Hitachi S-4800, Phillips Analytical FEI Tecnai30 and FEI Titan G2. The XAS measurements were performed at the BL14-W1 beamline at Shanghai Synchrotron Radiation Facility (SSRF), and the measurements were conducted in the transmission mode and Ni foil were used for energy calibration. The Ce L$_3$-edge X-ray absorption spectroscopy was collected in the transmission mode using inhouse laboratory-based X-ray absorption spectrometer. All XAFS data were analyzed using the program Demeter. The thermal conductivity detector (TCD) was used to perform H$_2$ temperature programmed reduction (H$_2$-TPR) experiments. The samples were pretreated for 1 h at 200 ℃ under the Ar (50 mL/min). Furthermore, the samples were heated from room temperature to 800 ℃ under the atmosphere of 5% H$_2$/Ar (30 mL/min). The temperature programmed surface reaction of methane (CH$_4$-TPSR) was performed using a homemade device. Initially, 100 mg of the catalyst underwent pretreatment in Ar flow (40 mL·min^{-1}) at 200 ℃ for 1 h. Subsequently, following cooling to 30 ℃, the gas of CH$_4$ was introduced. CH$_4$ -TPSR experiments were performed from 30 ℃ to 900 ℃ at a ramp rate of 7 ℃/min. The reaction products were continuously monitored by a mass spectrometry detector (Pfeiffer OmniStar GSD 320). The mass-to-charge ratio (m/z) of 16 was used as the mass spectrometry signal corresponding to the reactant CH$_4$, while m/z = 2 was assigned to signify the mass spectrometry signal of reaction products H$_2$. The experiment of CO$_2$ temperature-programmed desorption (CO$_2$-TPD) were performed on a homemade device. X-ray photoelectron spectra (XPS) were collected on a PHI Quantum 2000 XPS system with the C 1 s peak (284.6 eV) as a reference. The Ni loadings of samples were obtained by Inductive Coupled Plasma-Optical Emission Spectroscopy (ICP-OES) on a Thermo-Fisher icap 7000 system.

2.4. Catalytic performance measurement

Dry reforming of methane over the Ni$_1$@mp-CeO$_2$ catalysts were carried out in a fixed-bed quartz reactor. Briefly, ca. 50 mg of calcined catalysts (40–60 meshes) were placed in the center of the reactor using two pieces of thin quartz wool. A thermocouple was located at the end of catalyst bed to monitor the reaction temperature. Prior to the catalytic experiment, the samples were *in-situ* reduced at 500 ℃ for 1 h under H$_2$ flow, and then purged for 30 min with pure Ar. Subsequently, DRM reaction was conducted at 750 ℃ with a diluted-gas feeding gas of CH$_4$/CO$_2$/Ar (molar ratio = 1/1/3) at a total flow rate of 50 mL/min (weight hourly space velocity (WHSV) = 120 L/(g·h)). The flow rate of each gas was controlled by mass flow controller (D07–7B/ZM, Beijing Sevenstar Electronic Co., Ltd). The effluent gas was online analyzed by using gas chromatograph (GC2060, Shanghai Ruimin Chromatograph Instruments Co., Ltd.) equipped with a thermal conductivity detector (TCD) and a stainless-steel column packed with carbon molecular sieve (TDX-01). The conversions of CH$_4$, CO$_2$ and the H$_2$/CO molar ratio were calculated using the following equations:

$$\text{Conversion}_{CH_4} = \left(F_{CH_4,in} - F_{CH_4,out}\right) / F_{CH_4,in} \times 100\% \tag{1}$$

$$\text{Conversion}_{CO_2} = \left(F_{CO_2,in} - F_{CO_2,out}\right) / F_{CO_4,in} \times 100\% \tag{2}$$

Molar Ratio H$_2$/CO = moles of H$_2$ produced / moles of CO produced
Kinetic data were determined by separate experiments, and the conversion of CH$_4$ and CO$_2$ was kept at < 15% to ensure the reaction

under the intrinsic kinetic regime. The effect of internal and external diffusion was also eliminated.

For the dry reforming of methane, the reaction rate is expressed as follows:

$$r_{CH_4} = k(P_{CH_4})^a \cdot (P_{CO_2})^b \qquad (3)$$

The activation energies were calculated according to Arrhenius equation:

$$\ln k = -\frac{E_a}{RT} + c \qquad (4)$$

The slope of the linear relationship of lnk and 1/T is -E$_a$/R, where E$_a$ refers to the apparent activation energy (J·mol^{-1}), R is the gas constant (J·mol^{-1}·K^{-1}), and T refers to the reactor temperature (K). Reaction rate as a function of the CH$_4$ or CO$_2$ partial pressure was measured from 460 °C to 490 °C.

3. Results and discussion

3.1. Catalyst characterization

The XRD patterns (Figure S1) of the SBA-15 confirm that mesoporous silica SBA-15 are successfully synthesized. The as-synthesized SBA-15 was used as a hard template to synthesize the mesoporous CeO$_2$ (Fig. 1a). The ordered structure of mp-CeO$_2$ was evidenced by the TEM (Figure S2a-b) and small angle XRD (Figure S2c). The wide-angle XRD pattern of the mp-CeO$_2$ material (Figure S2d) matched well with the standard CeO$_2$ (JCPDS Card No.34–0394).[34] SEM-EDS results

(Figure S2f-h) and Table S1 indicated that only Ce and O elements were detected, with absence of Si element, indicating that the hard template SBA-15 was completely removed after NaOH leaching.

After trapping Ni single atoms, the obtained Ni$_1$@mp-CeO$_2$ catalyst maintained the ordered mesoporous structure of the mp-CeO$_2$ (Figure S3). The STEM and EDX-mapping of the Ni$_1$@mp-CeO$_2$ demonstrate that Ni species is highly dispersed on the mp-CeO$_2$ surface (Fig. 1b-c and Figure S4). The wide-angle XRD pattern of the Ni$_1$@mp-CeO$_2$ catalyst only displayed the diffraction peaks of CeO$_2$, evidencing the absence of crystalline NiO phases (Figure S5). For comparison, Ni supported on bulk CeO$_2$ also exhibited high dispersion (Fig. 1d, e and S6). X-ray absorption spectroscopy (XAS) has been utilized to investigate the coordination environment of nickel (Ni) atoms. Fig. 1f showed the Ni K-edge X-ray near-edge absorption spectra (XANES) of the as-synthesized Ni$_1$@mp-CeO$_2$ and Ni$_1$/CeO$_2$ catalysts. As compared to the reference samples, it indicated that the valence state of Ni species in Ni$_1$@mp-CeO$_2$ and Ni$_1$/CeO$_2$ is similar to NiO.[17,35,36] Furthermore, the X-ray absorption fine structure (EXAFS) spectra revealed the intense Ni-O scattering at 1.60 Å and a significant signal at 2.44 Å, which was attributed to the Ni-O-Ce scattering in both the as-synthesized Ni$_1$@mp-CeO$_2$ and Ni$_1$/CeO$_2$ catalysts (Fig. 1g, S7, and Table S2) [35,37]. These observations are consistent with the presence of atomically dispersed Ni on CeO$_2$ over the Ni catalysts supported on both mp-CeO$_2$ and bulk CeO$_2$, which aligns well with the AC-HAADF-STEM results (Fig. 1b, d). Additionally, the Ce L-edge XANES indicates a stronger interaction between the CeO$_2$ matrix and Ni species in as-synthesized Ni$_1$@mp-CeO$_2$ compared to Ni$_1$/CeO$_2$, as evidenced by the orbital interplay (Figure S8 and Table S3). Inductively coupled plasma optical
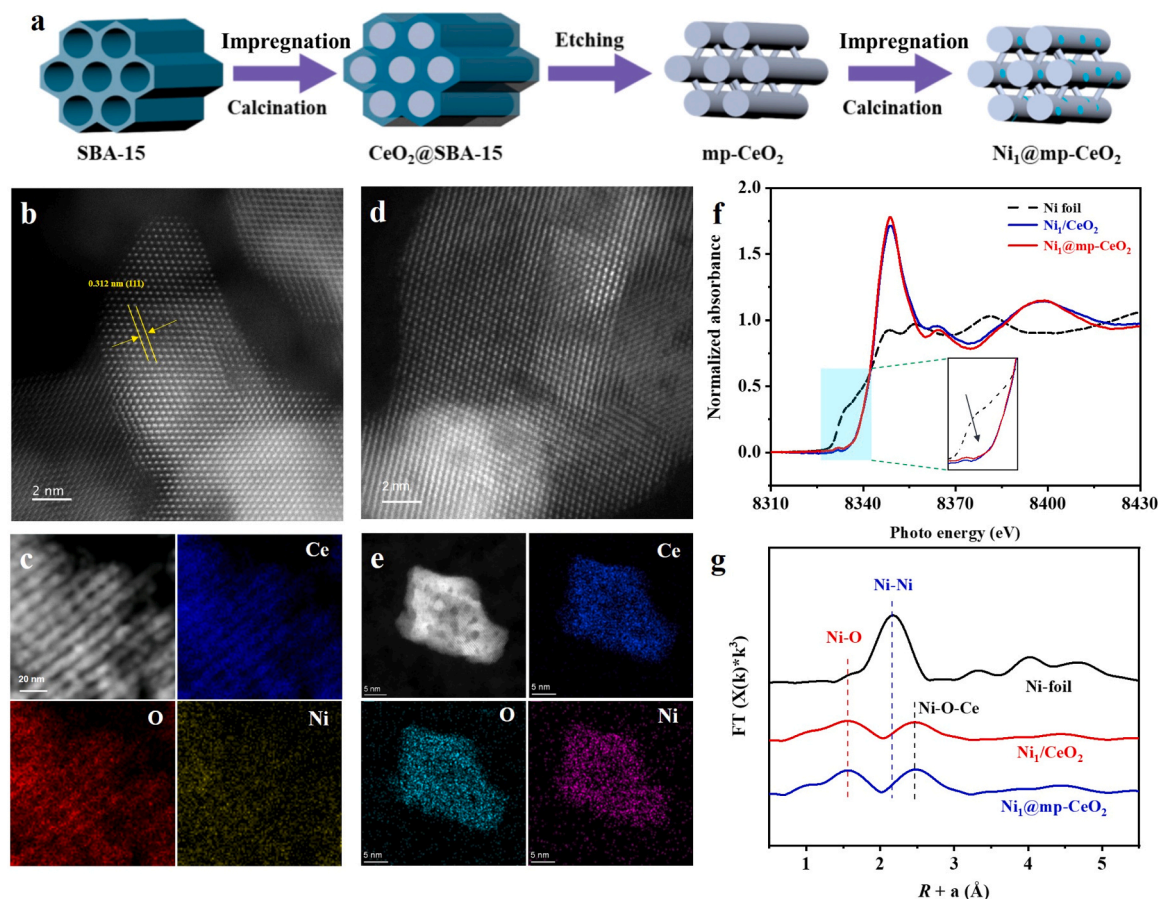

Fig. 1. (a) Schematic illustration of the synthetic routes of the as-prepared Ni$_1$@mp-CeO$_2$ catalyst, (b, d) AC-HAADF-STEM image of as-prepared Ni$_1$@mp-CeO$_2$ and as-prepared Ni$_1$/CeO$_2$, (c, e) STEM image and EDX mapping of as-prepared Ni$_1$@mp-CeO$_2$ and as-prepared Ni$_1$/CeO$_2$ catalysts (Ce, O, Ni). (f) The Ni K-edge XANES spectra and (g) The corresponding k^2-weighted Fourier transform extended X-ray absorption fine structure (EXAFS) spectra in R space of Ni foil, as-prepared Ni$_1$@mp-CeO$_2$, and as-prepared Ni$_1$/CeO$_2$ catalysts.

emission spectroscopy (ICP-OES) results indicated that the Ni content in $Ni_1@mp\text{-}CeO_2$ and Ni_1/CeO_2 was 2.1 wt% and 2.4 wt% (Table 1), respectively. Nitrogen adsorption-desorption measurements (Figure S9 and Table 1) show that the specific surface area of the as-prepared $Ni_1@mp\text{-}CeO_2$ ($98\ m^2/g$) was significantly higher than that of Ni_1/CeO_2 ($54\ m^2/g$).

Prior to the catalytic reaction, both $Ni_1@mp\text{-}CeO_2$ and Ni_1/CeO_2 catalysts were subjected to reduction in an H_2 atmosphere at 500 °C for 1 h. The wide-angle X-ray diffraction (XRD) pattern of the reduced catalysts only presented the typical structure of CeO_2 and excluded the presence of the crystalline Ni or NiO phases (Figure S10a). Small-angle XRD of the reduced $Ni_1@mp\text{-}CeO_2$ confirmed the maintenance of the ordered mesoporous structure (Figure S10b). XAS and TEM characterizations were conducted to investigate the nature of the Ni species in the reduced catalysts. The Ni−O coordination in the reduced $Ni_1@mp\text{-}CeO_2$ catalyst was confirmed by Ni K-edge XANES spectra, while a significant decrease in reduced Ni_1/CeO_2 was observed (Fig. 2a, b). The EXAFS fitting curves and structures of the reduced $Ni_1@mp\text{-}CeO_2$ (Fig. 2b, S11, and Table S4) revealed two peaks at around 1.60 Å and 2.33 Å, attributed to Ni-O and Ni-Ce scattering, respectively, which were unambiguously observed in the case of $Ni_1@mp\text{-}CeO_2$[35]. In contrast, in the case of Ni_1/CeO_2, a Ni-Ni contribution at 2.17 Å was observed, indicating the presence of Ni-Ni coordination (Fig. 2b and Table S4). Additionally, the Ce L-edge XANES indicated that the Ce^{3+} proportion in the reduced $Ni_1@mp\text{-}CeO_2$ was higher than that in Ni_1/CeO_2 (Figure S12 and Table S5). Fig. 2c and S13a showed that the $Ni_1@mp\text{-}CeO_2$ catalyst exhibited an ordered mesoporous structure and lattice fringe corresponding to the Ni (111) was seen at the interface, indicating that Ni single atoms on mp-CeO_2 were evolved into small clusters (~ 2.2 nm) under reducing conditions (Figure S14). Likewise, HR-TEM images of the reduced Ni_1/CeO_2 catalyst (Fig. 2d and S13b) showed that the Ni species with the average size of 4.5 nm were deposited on the CeO_2 powder after reduction. N_2O pulse titration measurement evidenced the higher Ni dispersion in the $Ni_1@mp\text{-}CeO_2$ and the smaller size of the clusters as compared to Ni_1/CeO_2 (Table 1 and Table S6).

3.2. Catalytic performances

The catalytic performances of the reduced $Ni_1@mp\text{-}CeO_2$ and Ni_1/CeO_2 catalysts were evaluated in dry reforming of methane (DRM) at the temperature of 750 °C. The $Ni_1@mp\text{-}CeO_2$ catalyst exhibited high catalytic stability in DRM with a slight decrease in performance over a 40 h run, achieving high conversion of CH_4 and CO_2 of approximately 91% and 90%, respectively (Fig. 3 and Figure S15). The H_2/CO ratio of $Ni_1@mp\text{-}CeO_2$ remained stable at 0.86 for the full process (Figure S15a). In contrast, the Ni_1/CeO_2 catalyst (Fig. 3a and Figure S15c) displayed lower initial activity than $Ni_1@mp\text{-}CeO_2$ and rapid deactivation in the DRM, showing a decrease of CH_4 conversion from 87% to 38% and the CO_2 conversion from 86% to 48% after 27 h of the reaction. The deactivation kinetic constants (k_d) for CH_4 on the $Ni_1@mp\text{-}CeO_2$ and Ni_1/CeO_2 catalysts were $0.2*10^{-3}$ and $23.3*10^{-3}\ h^{-1}$ (Fig. 3b), respectively,

indicating that the former has a lower deactivation rate by 2 orders of magnitude than the latter. The $Ni_1@mp\text{-}CeO_2$ catalyst also exhibited a lower deactivation kinetic constant (k_d) of CO_2 ($0.1*10^{-3}\ h^{-1}$) than Ni_1/CeO_2 ($9.6*10^{-3}\ h^{-1}$) (Figure S15d). Therefore, the Ni single atoms supported on bulk CeO_2 showed poor stability in the DRM, compared to the mesoporous CeO_2 trapped Ni single atoms. We have also synthesized the Ni_1/CeO_2-rod catalyst the result revealed that the reactivity of Ni_1/CeO_2-rod catalyst is superior to the Ni_1/CeO_2 catalyst, but lower than the $Ni_1@mp\text{-}CeO_2$ catalyst (Figure S15). The apparent activation energy (Ea) of the two Ni SAC was estimated. To obtain the differential mass-normalized reaction rates in the kinetic regime, the CH_4 conversions were controlled at < 15% where the effect of heat and mass transfer was excluded. As shown in Fig. 3c and Figure S15f, the Ea value for CH_4 of the Ni_1/CeO_2 ($113.3\ kJ\cdot mol^{-1}$) is significantly higher than that of $Ni_1@mp\text{-}CeO_2$ catalyst ($72.9\ kJ\cdot mol^{-1}$).

The deactivation of catalysts in DRM was due to coke deposition and sintering of Ni species. Thermogravimetric analysis (TGA) curves of the spent catalysts (Fig. 3d) showed that Ni_1/CeO_2 had a large amount of carbon deposition with the carbon deposition rate of $9.33*10^{-5}$ $g\cdot g_{cat}^{-1}\cdot h^{-1}$, as compared to $4.75*10^{-5}\ g\cdot g_{cat}^{-1}\cdot h^{-1}$ for the $Ni_1@mp\text{-}CeO_2$ catalyst. The lower carbon deposition rate on the $Ni_1@mp\text{-}CeO_2$ catalyst is ascribed to the large number of oxygen vacancies in mp-CeO_2, effectively activating CO_2 and facilitating the elimination of carbon deposits. The $Ni_1@mp\text{-}CeO_2$ catalyst remained stable without significant deactivation for 120 h under reactive conditions (Fig. 3e), which is attributed to the strong metal-support interaction and confinement effect.

The EXAFS spectra of the spent $Ni_1@mp\text{-}CeO_2$ and Ni_1/CeO_2 catalysts revealed the presence of Ni-Ni coordination, indicated by the presence of the Ni-Ni peak in the spectra (Figure S16-17). However, the Ni K-edge XANES collected for the spent $Ni_1@mp\text{-}CeO_2$ and Ni_1/CeO_2 catalysts showed distinct differences. Ni_1/CeO_2 exhibits an intense white line similar to that of Ni foil, suggesting a metallic chemical state. In contrast, $Ni_1@mp\text{-}CeO_2$ displays a higher white line and a strong pre-edge feature far away from Ni foil, indicating an oxidized chemical state (Figure S16). The results of XAS confirmed that the valence of Ni species in $Ni_1@mp\text{-}CeO_2$ is higher than that in Ni_1/CeO_2, and means the size of Ni species is much smaller in the $Ni_1@mp\text{-}CeO_2$ compared to that in the Ni_1/CeO_2. TEM images of the spent catalysts (Figure S19a-b) showed the absence of the large Ni particles on mp-CeO_2, demonstrating that Ni species did not undergo considerable sintering. On the contrary, Ni species on the Ni_1/CeO_2 catalysts tended to agglomerate into larger Ni NPs (from 4.5 nm to 11.2 nm) under the reaction conditions (Figure S19c-d), accompanied by the presence of coke and carbon nanotubes (Figure S19c). These carbon species blocked the active sites, resulting in the rapid deactivation of the catalyst during DRM.

The above observation aligns with the previous results that carbon or coke were prone to form over the large nickel particles during DRM [17, 38,39]. Methane activation in DRM is dimensionally sensitive, as CH_4 preferentially dissociates on smaller Ni clusters, whereas the ordered mesoporous structure of mp-CeO_2 has a spatially confinement effect, and the strong interaction between metal and support inhibited the sintering of active components. As a result, the catalytic activity and

Table 1
Textural properties of Ni_1/CeO_2 and $Ni_1@mp\text{-}CeO_2$ catalysts.

Catalyst	Surface area[a]	Ni content[b]	Ni particle size (nm)		Relative concentration (%)[e]	
	(m^2/g)	(wt%)	Chemisorption[c]	TEM[d]	$\dfrac{O_\beta}{O_\alpha + O_\beta + O_\gamma}$	$\dfrac{Ce^{3+}}{Ce^{3+} + Ce^{4+}}$
Ni_1/CeO_2	54	2.4	8.6	4.5	27.8	23.3
$Ni_1@mp\text{-}CeO_2$	98	2.1	3.5	2.2	43.0	30.9

[a] Textural parameters were determined from nitrogen physisorption.
[b] Ni loading was determined by ICP-OES.
[c] Ni particle size was calculated by N_2O pulse titration.
[d] Average Ni particle sizes in reduced Ni catalysts were measured from 100 particles observed in TEM images.
[e] Relative concentration (%) was calculated by XPS analyses of the reduced Ni catalysts.
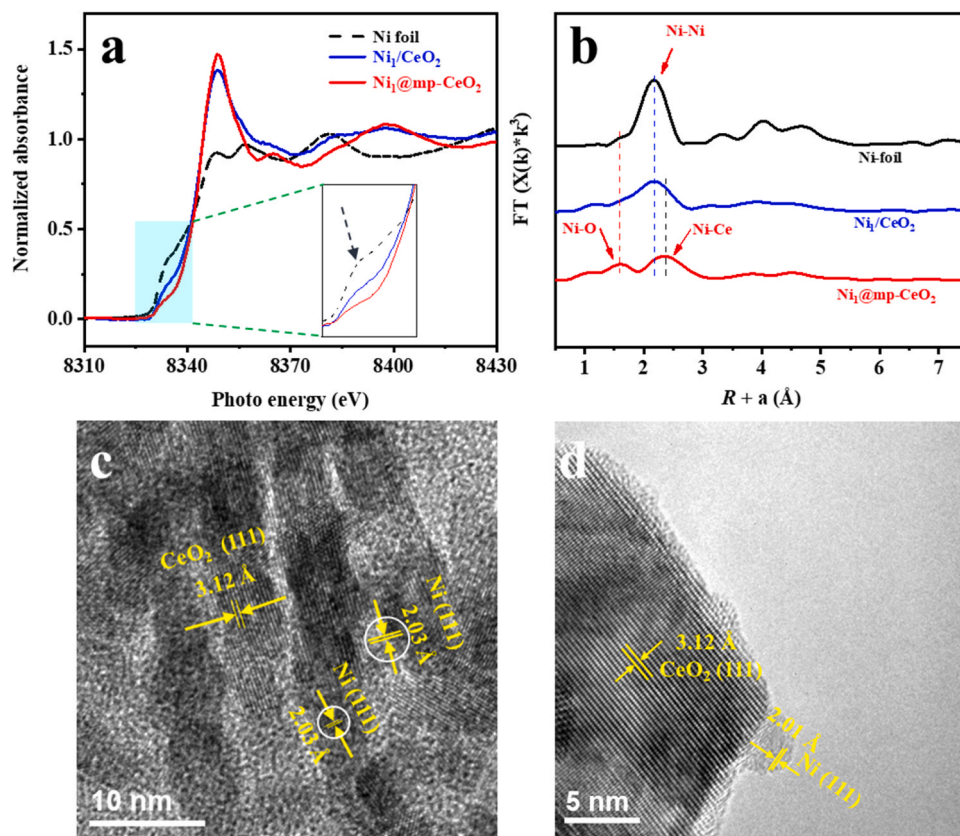
Fig. 2. (a) The Ni K-edge XANES spectra and (b) The corresponding k^2-weighted Fourier transform extended X-ray absorption fine structure (EXAFS) spectra in R space of Ni foil, $Ni_1@mp-CeO_2$, and Ni_1/CeO_2 after reduced. The representative TEM image of the reduced $Ni_1@mp-CeO_2$ (c) and Ni_1/CeO_2 (d) catalysts.

stability of $Ni_1@mp-CeO_2$ was much higher than that of Ni_1/CeO_2. The structure evolution of the two Ni single atom catalysts supported on CeO_2 in DRM is schematically shown in Fig. 3f-g.

The reducibility and the interaction between the metal species and oxide support over the $Ni_1@mp-CeO_2$ and Ni_1/CeO_2 catalysts were investigated via H_2-TPR (Fig. 4a). The results revealed significant differences in the reduction peak positions of the two catalysts, indicating the distinct degrees of interaction between Ni and support materials (mp-CeO_2 and bulk CeO_2). The main reduction peaks were observed in three temperature ranges: 150–280 °C, 300–550 °C and 700–850 °C. The low temperature reduction peak of 150–280 °C indicated the weak interaction between Ni species and CeO_2, while the reduction peak of 300–550 °C was associated with highly dispersed Ni species with a strong interaction with CeO_2. The 700–850 °C peak corresponded to the reduction of CeO_2 support from Ce^{4+} to Ce^{3+}. Notably, the main reduction peak of Ni species in $Ni_1@mp-CeO_2$ at 359 °C was larger than that of Ni/CeO_2, indicating highly dispersed Ni species at mp-CeO_2 with a strong metal-support interaction at the interface (Fig. 4a), while the Ni_1/CeO_2 catalyst exhibited large low-temperature reduction peaks at 261 °C and 310 °C, indicating weakly interacted between Ni species and bulk CeO_2.

The CO_2-TPD analysis depicted in Fig. 4b was utilized to evaluate the strength of the basic sites on the catalyst's surface. There are two major types of basic sites: (a) the peak between 90 °C and 230 °C, representing the weak basic sites, (b) the peak between 260 °C and 550 °C, corresponding to medium and strong basic sites. Since the weak basic sites didn't have a significant impact during DRM reaction, the difference in the weak CO_2 desorption over the reduced $Ni_1@mp-CeO_2$ and Ni_1/CeO_2 is therefore negligible (Table S9). For the $Ni_1@mp-CeO_2$ and Ni_1/CeO_2 catalyst, the primary desorption peak occurs at 260–550°C, medium and strong adsorption sites, were associated with the desorption of bidentate carbonates (B-CO_3*) from Ce^{4+}-O^{2-} and metal -O^{2-} pairs. This suggested

that $Ni_1@mp-CeO_2$ (77.6%) possessed a higher concentration of medium and strong basic sites compared to Ni_1/CeO_2 (48.8%), which is beneficial during the DRM reaction. The abundance of medium and strong basic sites on the $Ni_1@mp-CeO_2$ surface enhanced the adsorption and activation of CO_2, ultimately contributing improving the stability of DRM.

Fig. 4c displays the Raman spectra recorded for the $Ni_1@mp-CeO_2$ and Ni_1/CeO_2 catalysts, providing the information on the formation and concentration of oxygen vacancies. The peaks observed at around 240 cm^{-1}, 456 cm^{-1}, 573 cm^{-1}, and 1172 cm^{-1} correspond to the second-order transverse acoustic mode, the strong F_{2g} vibration mode of CeO_2 lattice, the defect-induced or oxygen vacancy-induced D mode and second-order longitude optical mode, respectively. Additionally, the intensity ratios of the D band and F_{2g} band (I_D/I_{F2g}) were calculated to reflect the degree of defect sites on CeO_2 and to evaluate the concentration of oxygen vacancies on these catalysts. The Raman spectra in Fig. 4c showed that the I_D/I_{F2g} value of $Ni_1@mp-CeO_2$ is 0.17, which is much higher than that of Ni_1/CeO_2 (0.09), demonstrating the more oxygen vacancies existed on $Ni_1@mp-CeO_2$. Previous studies have shown that the oxygen vacancies on catalyst surface can serve as the medium basic sites to promote the chemisorption and dissociation of CO_2 into CO and oxygen species [40–42]. The conclusion coincides with the results obtained from CO_2-TPD and DRM activity test.

The XPS characterization was employed to investigate the electronic structure and surface elemental compositions of the catalysts. In the Ce 3d spectrum (Fig. 4d), the peaks represent two types of Ce species, belonging to Ce $3d_{5/2}$ (u) at approximately 901.2 eV and Ce $3d_{3/2}$ (v) at around 882.8 eV. The peaks of u_0, u, u_1, u_2, u_3 are ascribed to the Ce^{4+} species in CeO_2, while the peaks of v_0, v, v_1, v_2, v_3 represent the Ce^{3+} species in Ce_2O_3. Table 1 shows that the Ce^{3+} proportion (the value of $Ce^{3+}/ (Ce^{3+} + Ce^{4+})$) in the $Ni_1@mp-CeO_2$ is 30.9%, which is higher than that in Ni_1/CeO_2 (23.3%), consistent with the result of the Ce L_3-
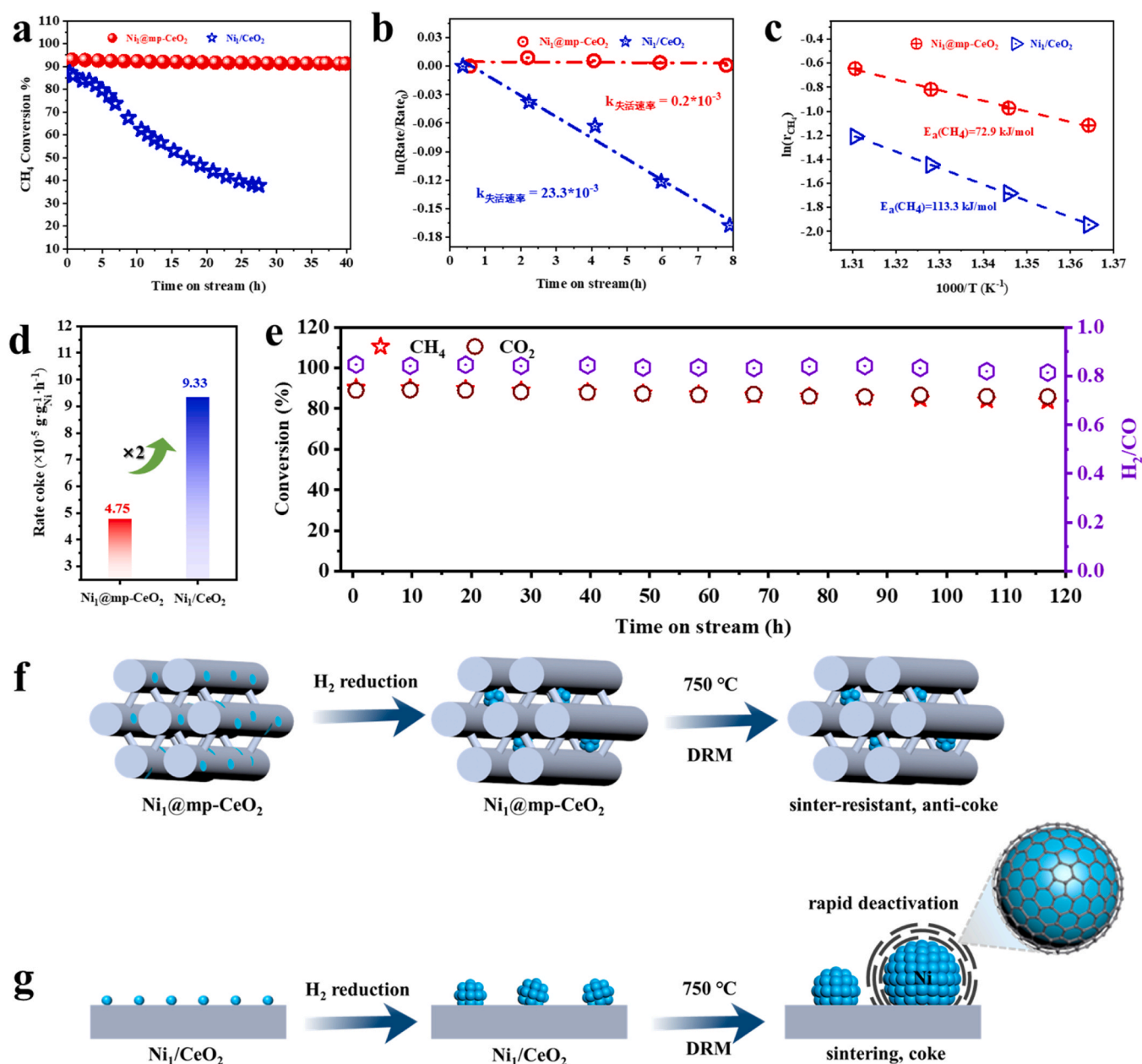
Fig. 3. The catalytic performance of the reduced $Ni_1@mp\text{-}CeO_2$ and Ni_1/CeO_2 at 750 °C: (a) CH_4 conversion. (b) Corresponding changes of CH_4 rates with respect to the initial rates (r/r_0); (c) Arrhenius plot; (d) TGA data of the spent catalysts after reaction. (e) Stability test of $Ni_1@mp\text{-}CeO_2$ catalyst in continuous DRM for 120 h. (f-g) Schematic illustration of the structure evolution of the two Ni single atom catalysts supported on bulk CeO_2 and mesoporous CeO_2 during the DRM.

edge XAFS spectra (Table S5). The positive shift in binding energy of Ce^{3+} from 882.8 to 883.0 eV is noticeable as a result of valence change from Ce^{4+} to Ce^{3+} in CeO_2. The chemical states of oxygen over the catalysts were analyzed by the O 1 s spectrum. Fig. 4e showed three types of oxygen species in the reduced catalysts. The peaks at 529.8 eV, 531.3 eV and 533.3 eV are attributed to the lattice oxygen (O_α), surface chemisorbed oxygen (O_β) and hydroxyl water and/or carbonates (O_γ) [43,44]. Furthermore, the $Ni_1@mp\text{-}CeO_2$ catalyst showed a relatively higher surface chemisorbed oxygen, and the ratio of $O_\beta/(O_\alpha+O_\beta+O_\gamma)$ is 43.0% which is much higher than that in Ni_1/CeO_2 (27.8%, Table 1). The Ni $2p_{3/2}$ XPS spectra in Fig. 4f show two types of Ni species at around 855.6 eV (Ni^{2+}) and 852.3 eV (Ni^0). The existence of Ni^{2+} species on the reduced Ni single-atom catalysts can be explained due to two issues. The first one is the unreduced Ni^{2+} species because of the strong metal-support interaction. The second one is that the reoxidation of active Ni metals in air may happen during sample preparation [45]. The

Ni^{2+} percentage on $Ni_1@mp\text{-}CeO_2$ surface was much higher than that on Ni_1/CeO_2 (Table S10), meanings the unreduced Ni species were embedded in the mp-CeO_2 channel, confirmed by H_2-TPR.

We further conducted the kinetic study of $Ni_1@mp\text{-}CeO_2$ and Ni_1/CeO_2 for the DRM reaction, analyzing the relationship between the reaction rates of methane and the partial pressure of CH_4 and CO_2 (Figure S20). The corresponding kinetic parameters (reaction orders, a and b) are presented in Table S11, indicating the dependence of the reaction rate on partial pressure of components. Our results demonstrate that the reaction rate is influenced by the partial pressures of both CH_4 and CO_2, with methane having a greater impact on the reaction kinetics, consistent with the previous study [46]. Notably, the reaction order (Figure S21) for $Ni_1@mp\text{-}CeO_2$ (a = 0.81, b = −0.07) are the same as those for Ni_1/CeO_2, suggesting that the reaction rate of both catalysts is affected by the partial pressure of reactants to the same degree. Additionally, Table S11 showed that the rate constant (k) for $Ni_1@mp\text{-}CeO_2$
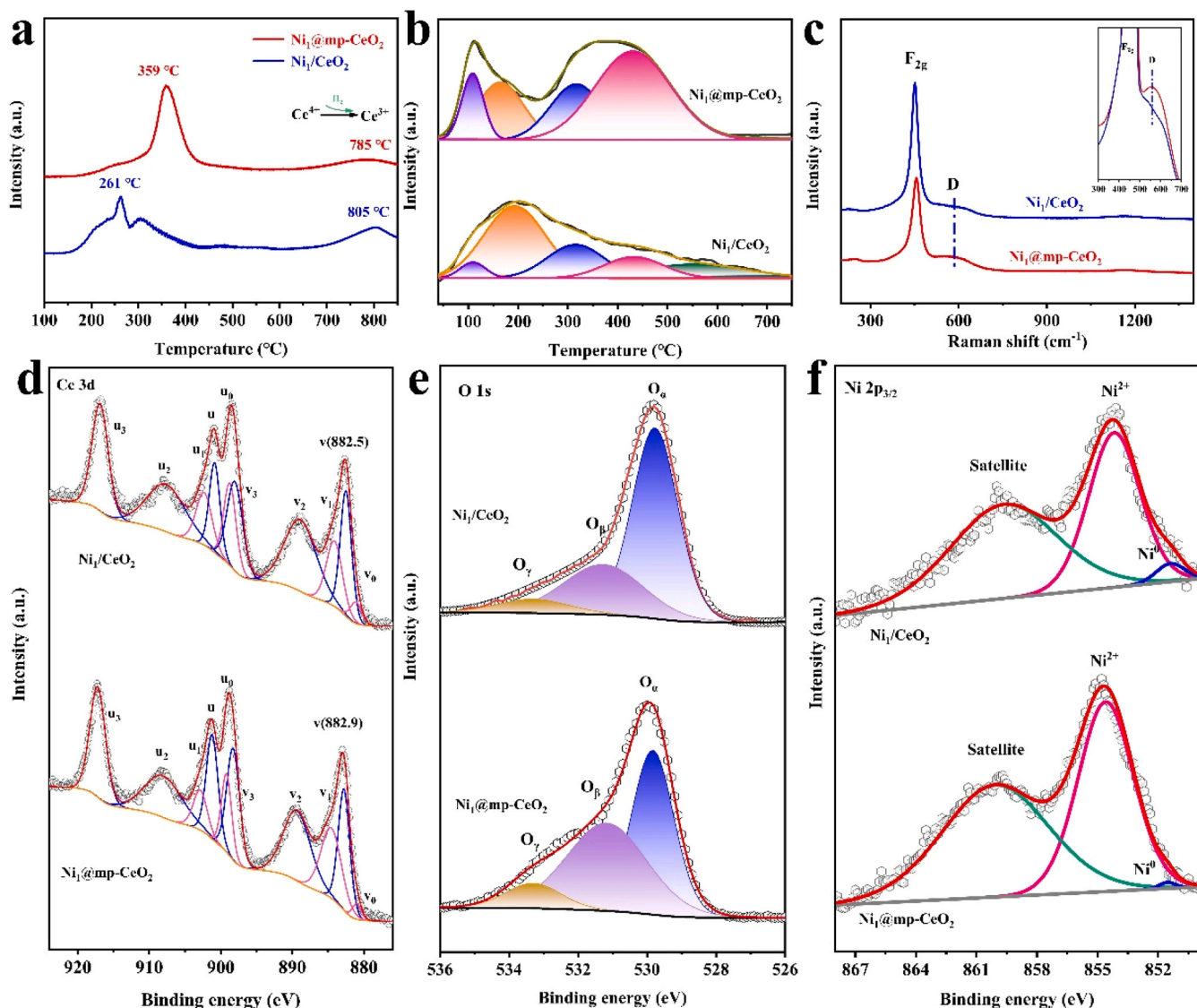
Fig. 4. (a) H_2-TPR profiles, (b) CO_2-TPD profiles and (c) Raman spectra of the fresh Ni_1@mp-CeO_2 and Ni_1/CeO_2, XPS spectra of (d) Ce 3d, (e) O 1 s and (f) Ni $2p_{3/2}$ over reduced Ni_1@mp-CeO_2 and Ni_1/CeO_2 catalysts.

is $18.0*10^{-2}$, significantly higher than that of Ni_1/CeO_2 ($7.7*10^{-2}$).

To gain insight into the coke resistance mechanism, we performed a series of temperature-programmed surface reactions. Efficient activation of C-H bonds of methane on Ni catalyst is a crucial step during DRM, therefore, *In-situ* experiments of TPSR-MS were performed by introducing CH_4 to investigate this process. Figure S22 showed the initial consumption of CH_4 on both Ni_1@mp-CeO_2 and Ni_1/CeO_2 catalysts was at 479 °C and 435 °C, respectively, accompanying by the formation of the deep decomposition product H_2 ($CH_4 \rightarrow C + H_2$), indicating that both catalysts can effectively activate methane even at low temperature (< 500 °C). However, no methane consumption was observed when the temperature was above 750 °C, meanings that these catalysts underwent rapid deactivation in CH_4 at high temperature, resulting from the encapsulation of the Ni active site by the dissociated carbon species from methane.

The CO_2-TPSR experiments provided insights into the CO_2 activation and coke removal abilities over the Ni_1@mp-CeO_2 and Ni_1/CeO_2 catalysts after treatment in CH_4-TPSR. Fig. 5a demonstrated that both catalysts exhibited CO_2 consumption at different temperatures, accompanying by the formation of CO in the product (Fig. 5b). This process was facilitated by the presence of oxygen vacancies (O_V), which

activated the CO_2 and facilitated its reaction with carbon species, resulting in the production of CO ($CO_2 + C \rightarrow 2CO$). The presence of the CO signal indicated the involvement of reactive oxygen species in the reaction, underscoring the role of O_V in the process. Specifically, CO was detected at 452 °C on the Ni_1@mp-CeO_2 catalyst, compared to 498 °C on Ni_1/CeO_2 (insert Fig. 5b), highlighting the superior performance of Ni_1@mp-CeO_2 in terms of activity and carbon removal ability. Fig. 5c shows that the peak temperature differences between CH_4 activation and CO_2 assisted coke elimination decrease from 122.8 °C on Ni_1/CeO_2 to 76.1 °C on Ni_1@mp-CeO_2. The Ni_1@mp-CeO_2 catalyst, with a high concentration of O_V, demonstrated the ability to eliminate carbon deposits at lower temperatures. In contrast, the Ni_1/CeO_2 catalyst exhibited a higher temperature for CO generation, due to the existence the fewer O_V. The synergistic effect of Ov and transition metal has been applied in other reactions. [47–49]

The Raman characterization revealed important differences in the presence of carbon species on the spent single atom Ni_1@mp-CeO_2 and Ni_1/CeO_2 catalysts. The peaks at 1340 cm^{-1}, 1560 cm^{-1}, 2677 cm^{-1} and 2921 cm^{-1} were attributed to the D band, G band, D' band and G' band of the carbon deposits (Fig. 5d), respectively. Interestingly, the spent Ni_1@mp-CeO_2 did not present any peak of carbon deposits due to
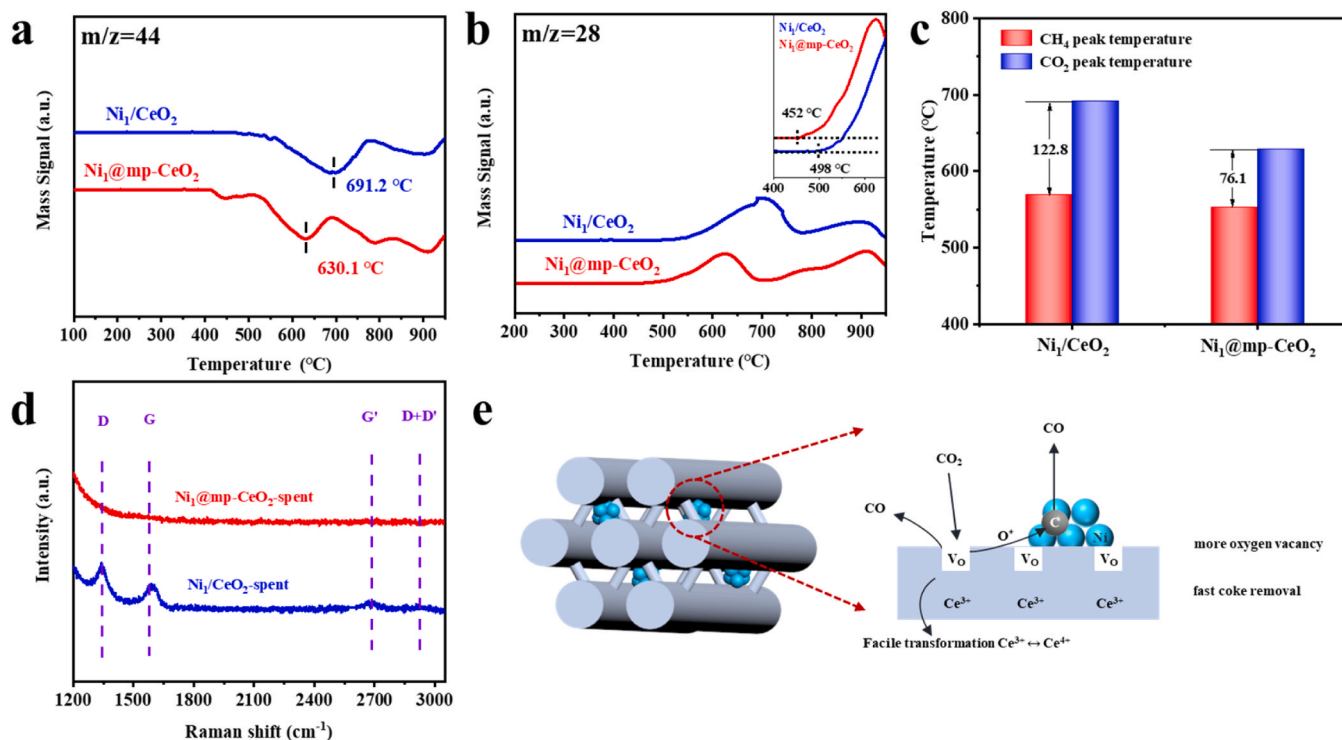
Fig. 5. The mass spectra with temperature programmed surface reaction (TPSR) for $Ni_1@mp\text{-}CeO_2$ and Ni_1/CeO_2 introduction of CO_2 after CH_4, (a) mass signal $m/z=44$, (b) mass signal $m/z=28$, (c) CH_4 and CO_2 consumption peak temperatures, (d) the Raman spectra after spent, and (e) the proposed mechanism of the removal of carbon species over $Ni_1@mp\text{-}CeO_2$ catalyst.

the large number of oxygen vacancies, while Ni_1/CeO_2 catalyst presented strong peaks (D and G bands) of carbon deposits, demonstrating that more O_V on the $Ni_1@mp\text{-}CeO_2$ led to the fast removal of carbon species (Fig. 5e) than Ni_1/CeO_2 SAC.

4. Conclusions

In this work, we focused on the structure evolution and catalytic performances of Ni single atoms trapped by ordered mesoporous CeO_2 ($mp\text{-}CeO_2$) in dry reforming of methane (DRM). The ordered mesoporous $mp\text{-}CeO_2$ was synthesized using SBA-15 silica as the hard template. It is seen that Ni single atoms were evolved into small Ni clusters on CeO_2 during DRM. The $mp\text{-}CeO_2$ presented high specific surface area, strong metal-support interaction due to the encapsulation structure, which prevented the sintering of Ni species during DRM at 750 °C. The $Ni_1@mp\text{-}CeO_2$ catalyst demonstrated high catalytic stability during the DRM test for up to 120 h. Compared with $Ni_1@mp\text{-}CeO_2$, the reference Ni_1/CeO_2 catalyst showed rapid deactivation with the conversion of CH_4 decreased from 87% to 38% and with higher carbon deposits observed.

The presence of more oxygen vacancy (O_V) and basic sites on the surface of $Ni_1@mp\text{-}CeO_2$ catalyst, contributes to the adsorption and activation of CO_2. The $Ni_1@mp\text{-}CeO_2$ catalyst exhibits good resistance to carbon deposition, mainly due to the sufficient CO_2 adsorption on basic sites. The presence of the O_V activated CO_2 and produced reactive oxygen species, eliminating the carbon species. A reference Ni_1/CeO_2 catalyst prepared via bulk CeO_2 showed fewer O_V, which produced a large amount of carbon species, leading to the pronounced deactivation during the DRM. These findings demonstrate that the combination of O_V, strong interaction between metal and support, and the mesoporous structure plays important roles in improving thermal stability and suppressing the coke formation when using Ni SAC as catalyst precursor, providing the valuable insight for the design of efficient catalysts with high activity and stability in DRM.

Author contributions

H.X. and J.L. conceived the research idea and designed the experiments. J.L. prepared all the samples and performed the structural characterizations and reactivity measurements. All authors discussed and commented on the manuscript.

CRediT authorship contribution statement

Qingyue Feng: Writing – review & editing, Investigation. **Min Hu:** Data curation. **Zizhen Zeng:** Writing – review & editing. **Zhun Zhang:** Data curation. **Hongxia Shen:** Writing – review & editing. **Yuxuan Zhang:** Software, Formal analysis. **Jianqiu Zhu:** Conceptualization, Writing – review & editing. **Linjuan Zhang:** Investigation, Resources, Software. **Wei Zhao:** Resources, Writing – review & editing. **Jiwei Li:** Writing – review & editing, Writing – original draft, Methodology, Investigation. **Jianyu Huang:** Writing – review & editing. **Congcong Du:** Writing – review & editing, Resources. **Haifeng Xiong:** Writing – review & editing, Supervision, Resources, Funding acquisition, Conceptualization. **Sixu Liu:** Software, Formal analysis. **Yiran Zhao:** Writing – review & editing, Software. **Junli Xu:** Writing – review & editing, Data curation.

Declaration of Competing interest

The authors declare that they have no known competing financial interests or personal relationships that could have appeared to influence the work reported in this paper.

Data availability

No data was used for the research described in the article.

Acknowledgments

Appendix A. Supporting information

Supplementary data associated with this article can be found in the online version at doi:10.1016/j.apcatb.2024.124069.

References

[1] J. Lin, A. Wang, B. Qiao, X. Liu, X. Yang, X. Wang, J. Liang, J. Li, J. Liu, T. Zhang, Remarkable performance of Ir$_1$/FeOx single-atom catalyst in water gas shift reaction, J. Am. Chem. Soc. 135 (2013) 15314–15317.

[2] H. Xiong, A.K. Datye, Y. Wang, Thermally stable single-atom heterogeneous catalysts, Adv. Mater. 33 (2021) 2004319.

[3] Y. Zhou, F. Wei, H. Qi, Y. Chai, L. Cao, J. Lin, Q. Wan, X. Liu, Y. Xing, S. Lin, A. Wang, X. Wang, T. Zhang, Peripheral-nitrogen effects on the Ru$_1$ centre for highly efficient propane dehydrogenation, Nat. Catal. 5 (2022) 1145–1156.

[4] N.J. LiBretto, Y. Xu, A. Quigley, E. Edwards, R. Nargund, J.C. Vega-Vila, R. Caulkins, A. Saxena, R. Gounder, J. Greeley, G. Zhang, J.T. Miller, Olefin oligomerization by main group Ga^{3+} and Zn^{2+} single site catalysts on SiO$_2$, Nat. Commun. 12 (2021) 2322.

[5] A.P. Valery Muravev, Yannis van den Bosch, Bianca Ligt, Nathalie Claes, Sara Bals, Nikolay Kosinov, Emiel J. M. Hensen, Size of cerium dioxide support nanocrystals dictates reactivity of highly dispersed palladium catalysts, Science 380 (2023) 1174–1178.

[6] Q. Zhang, X.X. Qin, F.P. Duan-Mu, H.M. Ji, Z.R. Shen, X.P. Han, W.B. Hu, Isolated platinum atoms stabilized by amorphous tungstenic acid: metal-support interaction for synergistic oxygen activation, Angew 57 (2018) 9351–9356.

[7] X. Xiong, C. Mao, Z. Yang, Q. Zhang, G.I.N. Waterhouse, L. Gu, T. Zhang, Photocatalytic CO$_2$ reduction to CO over Ni single atoms supported on defect-rich zirconia, Adv. Energy Mater. 10 (2020) 2002928.

[8] J. Wan, W. Chen, C. Jia, L. Zheng, J. Dong, X. Zheng, Y. Wang, W. Yan, C. Chen, Q. Peng, D. Wang, Y. Li, Defect effects on TiO$_2$ nanosheets: stabilizing single atomic site Au and promoting catalytic properties, Adv. Mater. 30 (2018) 1705369.

[9] H. Wei, X. Liu, A. Wang, L. Zhang, B. Qiao, X. Yang, Y. Huang, S. Miao, J. Liu, T. Zhang, FeOx-supported platinum single-atom and pseudo-single-atom catalysts for chemoselective hydrogenation of functionalized nitroarenes, Nat. Commun. 5 (2014) 5634.

[10] J. Jones, H. Xiong, A. DeLaRiva, E. Peterson, H. Pham, S. Challa, G. Qi, S. Oh, M. Wiebenga, X. Pereira Hernández, Y. Wang, A.K. Datye, Thermally stable single-atom platinum-on-ceria catalysts via atom trapping, Science 353 (2016) 6295.

[11] H. Liu, M. Cheng, Y. Liu, J. Wang, G. Zhang, L. Li, L. Du, G. Wang, S. Yang, X. Wang, Single atoms meet metal–organic frameworks: collaborative efforts for efficient photocatalysis, Energy Environ. Sci. 15 (2022) 3722–3749.

[12] L. Cao, W. Liu, Q. Luo, R. Yin, B. Wang, J. Weissenrieder, M. Soldemo, H. Yan, Y. Lin, Z. Sun, C. Ma, W. Zhang, S. Chen, H. Wang, Q. Guan, T. Yao, S. Wei, J. Yang, J. Lu, Atomically dispersed iron hydroxide anchored on Pt for preferential oxidation of CO in H$_2$, Nature 565 (2019) 631–635.

[13] H. Li, Q. Wan, C. Du, Q. Liu, J. Qi, X. Ding, S. Wang, S. Wan, J. Lin, C. Tian, L. Li, T. Peng, W. Zhao, K.H.L. Zhang, J. Huang, X. Zhang, Q. Gu, B. Yang, H. Guo, S. Lin, A.K. Datye, Y. Wang, H. Xiong, Vapor-phase self-assembly for generating thermally stable single-atom catalysts, Chem 8 (2022) 731–748.

[14] J. Yang, Y. Huang, H. Qi, C. Zeng, Q. Jiang, Y. Cui, Y. Su, X. Du, X. Pan, X. Liu, W. Li, B. Qiao, A. Wang, T. Zhang, Modulating the strong metal-support interaction of single-atom catalysts via vicinal structure decoration, Nat. Commun. 13 (2022) 4244.

[15] H. Xiong, D. Kunwar, D. Jiang, C.E. García-Vargas, H. Li, C. Du, G. Canning, X. I. Pereira-Hernandez, Q. Wan, S. Lin, S.C. Purdy, J.T. Miller, K. Leung, S.S. Chou, H.H. Brongersma, R. ter Veen, J. Huang, H. Guo, Y. Wang, A.K. Datye, Engineering catalyst supports to stabilize PdOx two-dimensional rafts for water-tolerant methane oxidation, Nat. Catal. 4 (2021) 830–839.

[16] J. Lee, S. Kang, E. Lee, M. Kang, J. Sung, T.J. Kim, P. Christopher, J. Park, D. H. Kim, Aggregation of CeO$_2$ particles with aligned grains drives sintering of Pt single atoms in Pt/CeO$_2$ catalysts, J. Mater. Chem. A 10 (2022) 7029–7035.

[17] M. Akri, S. Zhao, X. Li, K. Zang, A.F. Lee, M.A. Isaacs, W. Xi, Y. Gangarajula, J. Luo, Y. Ren, Y.T. Cui, L. Li, Y. Su, X. Pan, W. Wen, Y. Pan, K. Wilson, L. Li, B. Qiao, H. Ishii, Y.F. Liao, A. Wang, X. Wang, T. Zhang, Atomically dispersed nickel as coke-resistant active sites for methane dry reforming, Nat. Commun. 10 (2019) 5181.

[18] J. Yang, H. Qi, A. Li, X. Liu, X. Yang, S. Zhang, Q. Zhao, Q. Jiang, Y. Su, L. Zhang, J. F. Li, Z.Q. Tian, W. Liu, A. Wang, T. Zhang, Potential-driven restructuring of Cu single atoms to nanoparticles for boosting the electrochemical reduction of nitrate to ammonia, J. Am. Chem. Soc. 144 (2022) 12062–12071.

[19] D. Wu, S. Liu, M. Zhong, J. Zhao, C. Du, Y. Yang, Y. Sun, J. Lin, S. Wan, S. Wang, J. Huang, Y. Yao, Z. Li, H. Xiong, Nature and dynamic evolution of Rh single atoms trapped by CeO$_2$ in CO hydrogenation, ACS Catal. 12 (2022) 12253–12267.

[20] Q. Zhu, H. Zhou, L. Wang, L. Wang, C. Wang, H. Wang, W. Fang, M. He, Q. Wu, F.-S. Xiao, Enhanced CO$_2$ utilization in dry reforming of methane achieved through nickel-mediated hydrogen spillover in zeolite crystals, Nat. Catal. 5 (2022) 1030–1037.

[21] K. Bu, S. Kuboon, J. Deng, H. Li, T. Yan, G. Chen, L. Shi, D. Zhang, Methane dry reforming over boron nitride interface-confined and LDHs-derived Ni catalysts, Appl. Catal. B. 252 (2019) 86–97.

[22] K. Li, X. Chang, C. Pei, X. Li, S. Chen, X. Zhang, S. Assabumrungrat, Z.-J. Zhao, L. Zeng, J. Gong, Ordered mesoporous Ni/La$_2$O$_3$ catalysts with interfacial synergism towards CO$_2$ activation in dry reforming of methane, Appl. Catal. B. 259 (2019) 118092.

[23] J. Zhang, H. Wang, A.K. Dalai, Effects of metal content on activity and stability of Ni-Co bimetallic catalysts for CO$_2$ reforming of CH$_4$, Appl. Catal. A-Gen. 339 (2008) 121–129.

[24] Q. Cheng, X. Yao, L. Ou, Z. Hu, L. Zheng, G. Li, N. Morlanes, J.L. Cerrillo, P. Castaño, X. Li, J. Gascon, Y. Han, Highly efficient and stable methane dry reforming enabled by a single-site cationic Ni catalyst, J. Am. Chem. Soc. 145 (2023) 25109–25119.

[25] T. Montini, M. Melchionna, M. Monai, P. Fornasiero, Fundamentals and catalytic applications of CeO$_2$-based materials, Chem. Rev. 116 (2016) 5987–6041.

[26] Q. Wan, F. Wei, Y. Wang, F. Wang, L. Zhou, S. Lin, D. Xie, H. Guo, Single atom detachment from Cu clusters, and diffusion and trapping on CeO$_2$(111): implications in Ostwald ripening and atomic redispersion, Nanoscale 10 (2018) 17893–17901.

[27] Y. Tang, Y. Wei, Z. Wang, S. Zhang, Y. Li, L. Nguyen, Y. Li, Y. Zhou, W. Shen, F. F. Tao, P. Hu, Synergy of single-atom Ni$_1$ and Ru$_1$ sites on CeO$_2$ for dry reforming of CH$_4$, J. Am. Chem. Soc. 141 (2019) 7283–7293.

[28] H. Wang, J.X. Liu, L.F. Allard, S. Lee, J. Liu, H. Li, J. Wang, J. Wang, S.H. Oh, W. Li, M. Flytzani-Stephanopoulos, M. Shen, B.R. Goldsmith, M. Yang, Surpassing the single-atom catalytic activity limit through paired Pt-O-Pt ensemble built from isolated Pt$_1$ atoms, Nat. Commun. 10 (2019) 3808.

[29] Y. Xu, Z. Ding, Oxidation-induced and hydrothermal-assisted template-free synthesis of mesoporous CeO$_2$ for adsorption of acid orange 7, Materials 15 (2022) 5209.

[30] C. Cheng, F. Chen, H. Yi, G. Lai, CeO$_2$ mesoporous microspheres for high performance supercapacitors and lithium-ion batteries, J. Energy Storage 5 (2021) 102305.

[31] Y. Guo, Y. Gao, X. Li, G. Zhuang, K. Wang, Y. Zheng, D. Sun, J. Huang, Q. Li, Catalytic benzene oxidation by biogenic Pd nanoparticles over 3D-ordered mesoporous CeO$_2$, Chem. Eng. J. 362 (2019) 41–52.

[32] C. Wen, Y. Zhu, Y. Ye, S. Zhang, F. Cheng, Y. Liu, P. Wang, F.-F. Tao, Water-gas shift reaction on metal nanoclusters encapsulated in mesoporous ceria studied with ambient-pressure X-ray photoelectron spectroscopy, ACS Nano 6 (2012) 9305–9313.

[33] R. Ge, L.-Y. Dong, X. Hu, Y.-T. Wu, L. He, G.-P. Hao, A.-H. Lu, Intensified coupled electrolysis of CO$_2$ and brine over electrocatalysts with ordered mesoporous transport channels, Chem. Eng. J. 438 (2022) 135500.

[34] H. Zheng, W. Liao, J. Ding, F. Xu, A. Jia, W. Huang, Z. Zhang, Unveiling the key factors in determining the activity and selectivity of CO$_2$ hydrogenation over Ni/ CeO$_2$ catalysts, ACS Catal. 12 (2022) 15451–15462.

[35] Z. Rao, K. Wang, Y. Cao, Y. Feng, Z. Huang, Y. Chen, S. Wei, L. Liu, Z. Gong, Y. Cui, L. Li, X. Tu, D. Ma, Y. Zhou, Light-reinforced key intermediate for anticoking to boost highly durable methane dry reforming over single atom Ni active sites on CeO$_2$, J. Am. Chem. Soc. 145 (2023) 24625–24635.

[36] M. Akri, A. El Kasmi, C. Batiot-Dupeyrat, B. Qiao, Highly active and carbon-resistant nickel single-atom catalysts for methane dry reforming, Catalysts 10 (2020) 630.

[37] J. Wu, J. Gao, S. Lian, J. Li, K. Sun, S. Zhao, Y.D. Kim, Y. Ren, M. Zhang, Q. Liu, Z. Liu, Z. Peng, Engineering the oxygen vacancies enables Ni single-atom catalyst for stable and efficient C-H activation, Appl. Catal. B 314 (2022) 121516.

[38] S. Tang, L. Ji, J. Lin, H.C. Zeng, K.L. Tan, K. Li, CO$_2$ Reforming of methane to synthesis gas over sol–gel-made Ni/γ-Al$_2$O$_3$ catalysts from organometallic precursors, J. Catal. 194 (2000) 424–430.

[39] G.S. Gallego, F. Mondragón, J. Barrault, J.-M. Tatibouët, C, Batiot-Dupeyrat, CO$_2$ reforming of CH$_4$ over La–Ni based perovskite precursors, Appl. Catal. A-Gen. 311 (2006) 164–171.

[40] Z. Liu, D.C. Grinter, P.G. Lustemberg, T.D. Nguyen-Phan, Y. Zhou, S. Luo, I. Waluyo, E.J. Crumlin, D.J. Stacchiola, J. Zhou, J. Carrasco, H.F. Busnengo, M. V. Ganduglia-Pirovano, S.D. Senanayake, J.A. Rodriguez, Dry reforming of methane on a highly-active Ni-CeO$_2$ catalyst: effects of metal-support interactions on C–H bond breaking, Angew 55 (2016) 7455–7459.

[41] L.R. Winter, R. Chen, X. Chen, K. Chang, Z. Liu, S.D. Senanayake, A.M. Ebrahim, J. G. Chen, Elucidating the roles of metallic Ni and oxygen vacancies in CO$_2$ hydrogenation over Ni/CeO$_2$ using isotope exchange and in situ measurements, Appl. Catal. B. 245 (2019) 360–366.

[42] L. Chen, I.A.W. Filot, E.J.M. Hensen, Elucidation of the reverse water–gas shift reaction mechanism over an isolated Ru atom on CeO$_2$(111), J. Phys. Chem. C 127 (2023) 20314–20324.

[43] X. Liu, J. Ding, X. Lin, R. Gao, Z. Li, W.-L. Dai, Zr-doped CeO$_2$ nanorods as versatile catalyst in the epoxidation of styrene with tert-butyl hydroperoxide as the oxidant, Appl. Catal. A: Gen. 503 (2015) 117–123.

[44] D. Jampaiah, T. Srinivasa Reddy, A.E. Kandjani, P.R. Selvakannan, Y.M. Sabri, V. E. Coyle, R. Shukla, S.K. Bhargava, Fe-doped CeO$_2$ nanorods for enhanced peroxidase-like activity and their application towards glucose detection, J. Mater. Chem. B 4 (2016) 3874–3885.

[45] R.-P. Ye, Q. Li, W. Gong, T. Wang, J.J. Razink, L. Lin, Y.-Y. Qin, Z. Zhou, H. Adidharma, J. Tang, A.G. Russell, M. Fan, Y.-G. Yao, High-performance of nanostructured Ni/CeO$_2$ catalyst on CO$_2$ methanation, Appl. Catal. B 268 (2020) 118474.

[46] T. Zhang, Z. Liu, Y.-A. Zhu, Z. Liu, Z. Sui, K. Zhu, X. Zhou, Dry reforming of methane on Ni-Fe-MgO catalysts: influence of Fe on carbon-resistant property and kinetics, Appl. Catal. B. 264 (2020) 118497.

[47] Y. Bai, X. Zong, C. Jin, S. Wang, S. Wang, Synergy of single-atom Fe1 and Ce–Ov sites on mesoporous CeO$_2$–Al$_2$O$_3$ for efficient selective catalytic reduction of NO with CO, ACS Catal. 14 (2024) 827–836.

[48] N.H.M.D. Dostagir, R. Rattanawan, M. Gao, J. Ota, J.-y Hasegawa, K. Asakura, A. Fukouka, A. Shrotri, Co Single atoms in ZrO$_2$ with inherent oxygen vacancies for selective hydrogenation of CO$_2$ to CO, ACS Catal. 11 (2021) 9450–9461.

[49] R. Ye, L. Ma, J. Mao, X. Wang, X. Hong, A. Gallo, Y. Ma, W. Luo, B. Wang, R. Zhang, M.S. Duyar, Z. Jiang, J. Liu, A Ce-CuZn catalyst with abundant Cu/Zn-OV-Ce active sites for CO$_2$ hydrogenation to methanol, Nat. Commun. 15 (2024) 2159.